Letter

Mechanism of stochastic resonance in viscoelastic channel flow

Yuke Li*
College of Shipbuilding Engineering, Harbin Engineering University, Harbin 150001, China; Department of Physics of Complex Systems, Weizmann Institute of Science, Rehovot 7610001, Israel; and National Key Laboratory of Ship Structural Safety, Harbin 150001, China

Victor Steinberg†
Department of Physics of Complex Systems, Weizmann Institute of Science, Rehovot 7610001, Israel

(Received 11 May 2024; accepted 22 July 2025; published 25 August 2025)

Stochastic resonance (SR), the phenomenon discovered more than 40 years ago in bistable nonlinear dynamical systems in the presence of weak periodic forcing and external noise, results in strong amplification of the periodic signal, though at shifted frequency. Recently we reported the SR discovery in inertialess viscoelastic channel flow just above pure elastic instability onset in a limited lower subrange of the transition chaotic flow regime, where a sharp high-energy peak in the streamwise velocity chaotic power spectrum, E_u, is observed unexpectedly. The spanwise velocity power spectrum, E_w, remains flat, indicating white noise, and is accompanied by weak intensity elastic waves. These three necessary conditions for the SR emergence are consistent with those found in autonomous deterministic dynamical systems exhibiting deterministic stochastic resonance (DSR). Notably, DSR disappears in the upper subrange of the transition regime, where E_w becomes chaotic followed by strongly increased elastic wave intensity. Here we clarify the mechanism of DSR emergence by experimentally verifying three key ingredients of the DSR mechanism: chaotic E_u, flat white noise E_w, and weak elastic waves at multiple channel locations. Finally, we present a DSR existence range as a function of Wi and $u_{\rm rms}$, the root mean square of streamwise velocity fluctuations along the channel length, as another control parameter.

DOI: 10.1103/yv5x-261v

In recent publications we have reported a direct transition from laminar to sustained chaotic flow at $\mathrm{Wi} > \mathrm{Wi}_c$ and $\mathrm{Re} \ll 1$ in inertialess viscoelastic channel flow [1–4], which occurs despite the proven linear stability at the limit of low inertia of three-dimensional (3D) viscoelastic parallel streamline shear flows utilizing Oldroyd-B and Maxwell models [5–8]. Here, the Weissenberg number $\mathrm{Wi} = U\lambda/d$ is the main control parameter in inertia-free viscoelastic fluid flow, denoting the ratio of the elastic stress to its relaxation dissipation, and $\mathrm{Re} = \rho U d/\eta$ is the Reynolds number, where U is the mean flow velocity defined by the fluid discharge rate, λ is the longest polymer relaxation time, d is the characteristic vessel size, ρ is the fluid density, and η is the fluid viscosity. $\mathrm{Wi}_c = 150 \pm 10$ is the instability onset for the discussed channel [4]. The continuous elastic instability occurs via unstable nonorthogonal quasieigenmodes of the non-Hermitian linearized equation of polymeric constitutive equations at Wi_c [1–4] due to external noise, $u_{\rm rms}$, at the inlet ($l/h = 0$), where $u_{\rm rms}$ is the root mean square (rms) of the streamwise velocity fluctuations u', l is

*Contact author: yuke.li@hrbeu.edu.cn
†Contact author: victor.steinberg@weizmann.ac.il

the location along the channel, and h is the channel height. The observed continuous instability is distinct from the classical subcritical scenario in the Newtonian channel and pipe flows, where both laminar flow and turbulence can coexist above the nonmodal instability onset $\mathrm{Re_c}$ [9], contrary to our recent experimental observations [1–4,10]. Indeed, once Wi exceeds Wi_c, the channel flow becomes chaotic along the channel downstream until the outlet, and no saddle point or hysteresis is found in measurements of flow properties. However, in a sharp contradiction to the experimental results [1–4], recent analysis and numerical simulations, conducted by two groups in two-dimensional (2D) viscoelastic channel flow with 2D perturbations at $\mathrm{Re} \ll 1$ and $\mathrm{Wi} \gg 1$, reveal a linear normal mode instability. Moreover, one group has got the linear instability for unrealistic extremely dilute polymer solutions [11], whereas another group has added a diffusion term with an orders of magnitude larger diffusion coefficient than obtained in the experiments, to stabilize numerical calculations [12–14]. However, recently 3D numerical simulations employing the simplified Phan-Thien-Tanner model disclose a completely different scenario: a direct transition to chaotic flow, of which instability can occur only via nonorthogonal modes [15]. This finding aligns with our experimental results discussed above.

In viscoelastic channel flows, the key challenge is to uncover the mechanism promoting chaotic flow above Wi_c. In polymer solution flows with curvilinear streamlines, elastic instability and the subsequent growth of elastic stress with increasing Wi value are consequences of hoop stress, causing a radial bulk force responsible for a linear instability [16–18]. Nevertheless, this mechanism becomes ineffective in viscoelastic parallel shear flows [17]. Recently, we have proposed and experimentally verified the amplification mechanism of wall-normal fluctuating vortices by elastic waves, which resonantly pump energy taken out from the mean shear flow at $\mathrm{Wi} > \mathrm{Wi}_c$ [4]. However, in the close vicinity to Wi_c, where the elastic waves just appear, their intensity is insufficient to amplify vorticity fluctuations [2–4,18–20].

To elucidate experimentally the mechanism of a transition to chaotic flow in the close vicinity to Wi_c, we notably increase statistics of flow property measurements resulting in considerably higher resolution [21]. First, this Letter reveals two subranges at $\mathrm{Wi} > \mathrm{Wi}_c$ in the transition flow regime: lower at $150 < \mathrm{Wi} \leqslant 300$ and upper at $400 \leqslant \mathrm{Wi} \leqslant 1000$. In the lower subrange, the laminar flow becomes chaotic only for the streamwise velocity power spectrum E_u, while the spanwise velocity power spectrum E_w remains flat, indicating white noise, with low peak intensity of elastic waves. Thus, a cooperative interaction of chaotic spectrum E_u, white noise spectrum E_w, and weak elastic waves results in a coherently enhanced response realized here as stochastic resonance (SR) [21]. The evidence of SR shows up in the time series of $u(t)$ and pressure $p(t)$, where large and nearly periodic negative spikes are observed. These spikes are represented by high-intensity sharp peaks at low frequencies in E_u and pressure power spectra, E_p, in the lower subrange, which resemble SR, as suggested in Ref. [21], whereas, in the upper subrange, high-energy elastic waves take over the key role from SR to promote chaotic flow, since the former are able to amplify the wall-normal vorticity fluctuations and self-organize the streaks into cycles synchronized at the elastic wave frequency, f_{el} [4]. Thus, SR is the key element in the stochastic path to the persistent chaotic flow just above Wi_c in the lower subrange, although this finding is based only on the study of inertialess viscoelastic channel flow at the fixed spatial location $l/h = 380$ [21]. It represents an experimental observation of SR in chaotic systems within fluid dynamics. Furthermore, in the upper subrange at $400 \leqslant \mathrm{Wi} \leqslant 1000$, SR disappears along with the emergence of both E_u and E_w as chaotic power spectra and high intensity elastic waves.

The discovery of SR in the lower subrange above Wi_c is reminiscent of the emergence of deterministic SR (DSR) that appears in an autonomous deterministic dynamical chaotic system interacting with external white noise in the presence of a weak periodic modulation [22,23]. The DSR differs essentially from classical SR, which occurs in bistable nonlinear systems with two stable and one unstable equilibrium points, where external white noise randomly switches between two stable states in a double-well potential with a mean frequency depending on the height of the potential barrier and noise intensity. Then, adding to white noise a weak periodic signal results in SR. The classical SR is attracted outstanding interest due to the amplification of weak external oscillations by noise, contrary to the established opinion about suppression of weak oscillations by noise [24,25]. The deterministic dynamical chaotic system is characterized by structurally unstable chaotic quasiattractors very sensitive to external perturbations, which may result in SR due to weak periodic modulation. Above and near the vicinity of the chaotic quasiattractor merging crisis, random fluctuations cause intermittent hopping between two regions separated by the potential barrier due to interaction with external white noise, which is synchronized by weak periodic forcing of a limit cycle, generating DSR above the merging crisis [22,23].

Here we present experimental results obtained in the same inertialess viscoelastic channel flow and with the same approach as in Ref. [21], but instead at the single location $l/h = 380$, we collect data at multiple spatial locations, l/h, along the channel length. The main goal of the experiment is to verify the mechanism of DSR emergence and to validate the additional control parameter besides Wi, defining the DSR existence range as a function of $\mathrm{Wi} > \mathrm{Wi}_c$ and the channel location l/h, the second control parameter. Moreover, we intend to reveal the relation between elastic wave and DSR frequencies, an important feature to verify the proposed mechanism of the DSR emergence.

We performed the experiment in a long channel of dimensions 500 (L, x: streamwise) $\times$ 0.5 (h, y: wall-normal) $\times$ 3.5 (W, z: spanwise) mm^3, shown in Fig. S1 in the Supplemental Material [26]. The channel has two sources of finite-size perturbations, namely nonsmooth inlet and two 0.5-mm diameter holes in the top plate near the inlet and outlet used for pressure measurements. A dilute aqueous solution of 64% sucrose concentration and 80-ppm high molecular weight polyacrylamide is the same as used in Ref. [21]. The longest polymer relaxation time λ is 13 s. The average velocity U, used in both Wi and Re, is obtained via the flow discharge rate, Q, as $U = Q/\rho W h$. The details of the experimental setup and the working fluid rheological properties can be referred to in Ref. [26] and Refs. [27,28] therein. In the Methods section of Ref. [26], we present the details of the experimental setup, the preparation and characterization of the polymer solution, and the particle image velocimetry technique to measure the 2D velocity field in the x-z horizontal plane.

In Fig. 1, the left column shows three plots of the temporal evolution of $u^p_{\mathrm{rms}}(t)$, partially averaged over consecutive 1-s (100 samples) streamwise velocity fluctuations, at three positions, l/h: (a) 90 at $\mathrm{Wi} = 160$, (c) 180 at $\mathrm{Wi} = 228$, and (e) 960 at $\mathrm{Wi} = 172$. The right column shows $u(t)$ power spectra, E_u, in lin-log presentation at the corresponding l/h and various Wi values in the lower subrange of the transition flow regime: (b) 90 at $\mathrm{Wi} = 160$, (d) 180 at $\mathrm{Wi} = 164$ and 228, and (f) 960 at $\mathrm{Wi} = 155$, 172, and 250. In Figs. 1(a), 1(c), and 1(e), the $u^p_{\mathrm{rms}}(t)$ time evolution shows almost periodic spikes of the partially smoothed data, represented in E_u in Figs. 1(b), 1(d), and 1(f) by sharp, high-energy peaks associated with SR.

In Fig. S2 in Ref. [26] we show probability density functions (PDFs) of $P(u'/u_{\mathrm{rms}})$ at $l/h =$ 150 and 720 and several Wi values in the lower subrange of the transition flow regime. As in Ref. [21], strong deviations from the Gaussian PDF appear for negative values of u'/u_{rms} for all Wi. It is noteworthy that further down, the deviations of the left tail from the Gaussian PDF become closer to exponential than other shifted Gaussian PDFs, as observed at $l/h = 380$ in Fig. 5 in Ref. [21]. The characterization of the PDF shape deviation from Gaussian is quantified by its third and fourth moments, called skewness, S, and flatness (kurtosis), F, respectively, shown in Fig. 2(c) as a function of Wi values in the lower subregion over a wide range of l/h. At $l/h = 380$, 720, and 960, sufficiently far from the inlet, both S and F exhibit a nonmonotonic dependence on Wi with a smoothed maximum in the middle of the lower subrange, which decreases with increasing l/h. Meanwhile, at $l/h = 150$, F grows abruptly above Wi_c and then drops significantly towards $\mathrm{Wi} \approx 200$. The skewness (S) and the flatness (F) of the PDF (u'/u_{rms}) further confirm the boundary between two ranges at different l/h. The nonmonotonic dependency of S and F on Wi indicates at first growth and then decay of negative peaks in the PDF that witness the SR appearance.

As mentioned in the introduction and also in Ref. [21], at $l/h = 380$ DSR is observed only in the lower subrange. Indeed, as presented in Fig. 7(b) in Ref. [21], E_w in lin-log coordinates remains flat, indicating white noise, as a function of the normalized frequency, λf, with high intensity resolution and clear visible elastic wave peaks at six values of $\mathrm{Wi} > \mathrm{Wi}_c$ in the lower subrange, whereas E_w in log-log coordinates, at orders of magnitude lower resolution, reveals flat dependence on λf below

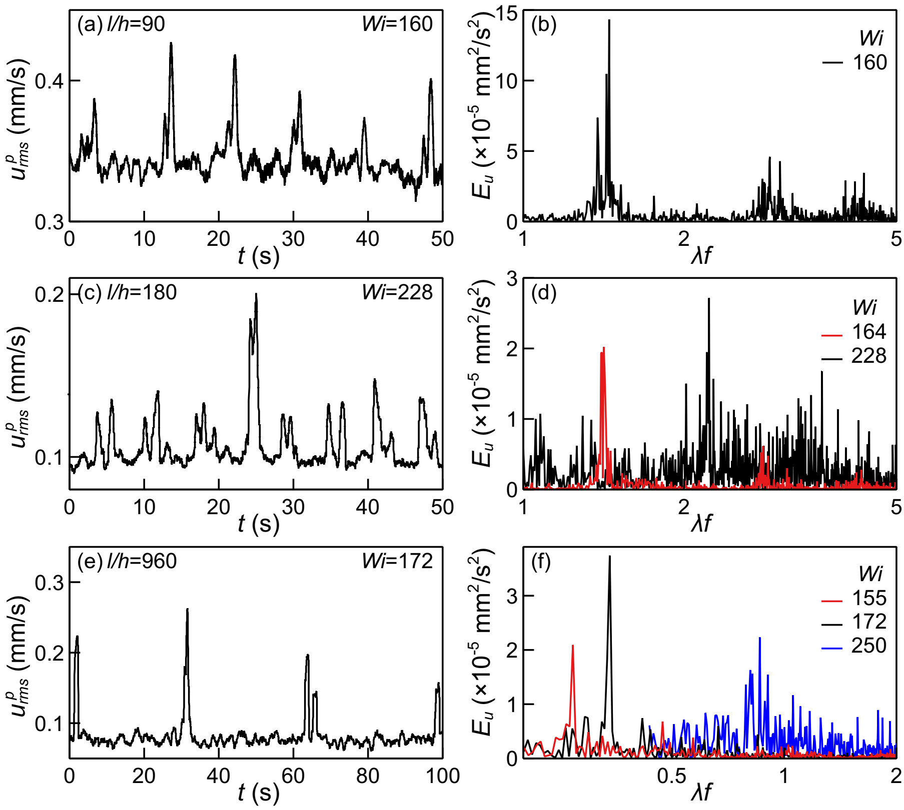

FIG. 1. Temporal evolution, partially averaged over consecutive 1-s (100 samples) streamwise velocity fluctuations, of $u^p_{\rm rms}(t)$, and u energy spectra, E_u, at various l/h and Wi values. At $l/h = 90$, (a) $u^p_{\rm rms}(t)$ at Wi = 160 and (b) E_u at Wi = 160; at $l/h = 180$, (c) $u^p_{\rm rms}(t)$ at Wi = 228 and (d) E_u at Wi = 164 and 228; at $l/h = 960$, (e) $u^p_{\rm rms}(t)$ at Wi = 172 and (f) E_u at Wi = 155, 172, and 250.

and above Wi_c in the lower subrange with unresolved elastic peaks, and changes to chaotic E_w in the upper subrange in Fig. 8 in Ref. [21]. According to the proposed similarity of the DSR appearance in the autonomous deterministic dynamical chaotic system [22,23], the interaction of the chaotic attractor with external white noise in the presence of weak oscillations is the necessary condition for the DSR emergence.

Furthermore, we present the DSR peak intensity, I_p, and its normalized frequency, λf_p, noticed exclusively in the lower subrange of the transition flow regime at ten locations, $l/h = 62$, 90, 150, 180, 270, 380, 635, 720, 840, and 960, and various Wi values, which are shown in Figs. 2(a) and 2(b) and also presented in Table S1 in Ref. [26]. Here, the DSR peak intensity, I_p, is obtained similarly to $I_{\rm el}$ by taking the peak height above the flat low frequency part of E_u [21]. The DSR normalized frequency, λf_p, grows with Wi at all locations, and the power-law fit of the data $\lambda f_p \sim (\mathrm{Wi} - \mathrm{Wi}_c)^\gamma$ discloses a scaling exponent $\gamma = 0.45 \pm 0.05$, the same as found at $l/h = 380$ in Ref. [21]. The I_p shows mostly growth with Wi for all l/h values, and then a slight decrease towards Wi ≈ 300, close to the upper limit of the lower subrange.

Similarly to the dependencies of I_p and λf_p as a function of Wi in the lower subrange at ten locations along the channel, discussed above, we plot $I_{\rm el}$ and $\lambda f_{\rm el}$ as a function of Wi, at 11 locations $l/h = 22$, 62, 90, 150, 180, 270, 380, 635, 720, 840, and 960 in both subranges of the transition flow regime, shown in Figs. S5(a) and S5(b) in Ref. [26]. In the lower subrange, E_w remains flat at intensity values from 10^{-8} to 10^{-7} mm^2/s^2 [see Fig. 3; see also Figs. S4(b)–S4(e) and Table S1 in

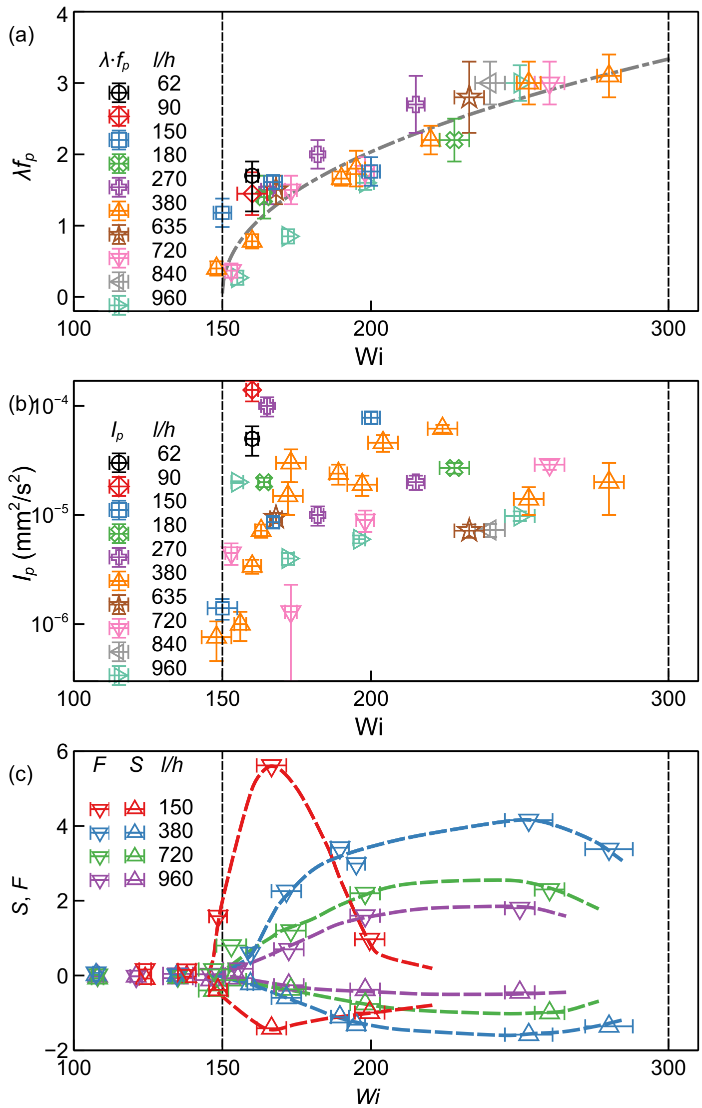

FIG. 2. Properties of spikes near threshold instability in two subranges. (a) Normalized SR frequency, λf_p, vs Wi at different l/h. The black dashed line is the power-law fit $\lambda f_p \sim (\mathrm{Wi} - \mathrm{Wi}_c)^\gamma$ with $\gamma = 0.45 \pm 0.05$. (b) SR peak energy I_p in E_u vs Wi at the same l/h. (c) Skewness, S, and flatness (kurtosis), F, of $P(u'/u_{\mathrm{rms}})$ vs Wi at four l/h values. The colored dashed lines show trends. The vertical black dashed lines in (a)–(c) mark $\mathrm{Wi}_c = 150$ and $\mathrm{Wi} = 300$, as the borders of the lower subrange.

Ref. [26]]. I_{el} intensity slowly increases but still remains below the resolution limit, marked by the red dotted line for all positions at $8 \times 10^{-8}\ \mathrm{mm}^2/\mathrm{s}^2$. Here I_{el} intensity is two orders of magnitude lower than I_p [see Fig. 2; see also Fig. S5(b) and Table S1 in Ref. [26]]. It is remarkable that in the lower subrange at $\mathrm{Wi}_c \leqslant \mathrm{Wi} < 300$ for all channel locations the I_{el} values are observed only below the red dashed line, and DSRs are revealed [see Figs. 2(a), 2(b), and 4; see also Fig. S5(b) in Ref. [26]]. However, at $l/h = 22$, I_{el} values are noticed above the red dotted line, and DSR disappears, whereas for $l/h = 62$ and 90, I_{el} values for both locations are found slightly below the

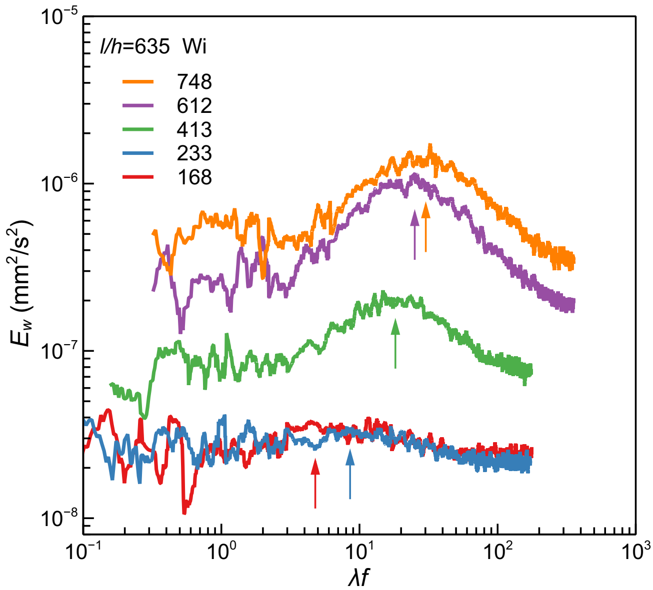

FIG. 3. Spanwise velocity energy spectra in log-log scale measured at the channel center far from the inlet: E_w at $l/h = 635$ and Wi = 168, 233, 413, 612, and 748. The arrows in the corresponding color are a guide for the weak and significant elastic waves in this log-log scale.

resolution limit at Wi = 162 and 160, and above it at Wi = 237 and 236, respectively, and DSRs are revealed only for the lower Wi values in Fig. S5(b) and Table S1 in Ref. [26].

In Fig. S5(a) in Ref. [26], we present the dependence of $\lambda f_{\rm el}$ on Wi at 11 positions along the channel. Despite a large scatter of $\lambda f_{\rm el}$ values due to low elastic wave intensity, $I_{\rm el}$, in the lower subrange of the transition flow regime, particularly at $l/h = 22, 62,$ and 90, the power-law fit $\lambda f_{\rm el} \sim ({\rm Wi} - 150)^{\beta}$ gives $\beta = 0.4 \pm 0.1$ [see Fig. S4(a) in Ref. [26]]. It is close to the exponent value $\gamma = 0.45 \pm 0.5$ obtained for λf_p in Fig. 2(a). In the upper subrange, E_w becomes chaotic with the power-law decay at high frequencies [see Fig. 3; see also Figs. S4(a), S4(b), and S4(c) in Ref. [26]], and the DSRs disappear. The latter is accompanied by the steep growth of $I_{\rm el}$, reaching the I_p values perceived in the lower subrange. The disappearance of the DSR peaks in E_u correlates with the growth of the elastic wave peak intensity $I_{\rm el}$, marking the breakdown of DSR. Thus, we show that the exponents β and γ in the scaling relations of $\lambda f_{\rm el}$ and λf_p versus ${\rm Wi} - {\rm Wi}_c$ have close

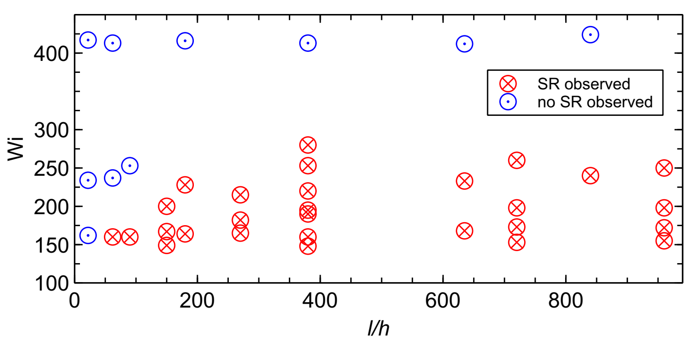

FIG. 4. Stochastic resonance peaks found in the lower subrange are shown in l/h and Wi coordinates.

exponent values 0.45 ± 0.5 and 0.4 ± 0.1, respectively, within the error bars, proving their direct relation. However, the range of λf_p is significantly shifted down up to five times compared to the range of λf_{el} [see Fig. 2(a) versus Fig. S4(a) in Ref. [26]].

To verify the dependence of E_w on λf at several channel locations, l/h, and various Wi in the whole transition flow regime, they are presented in log-log coordinates at $l/h = 635$ and $\mathrm{Wi} = 168, 233, 413, 612,$ and 748 in Fig. 3, and at several locations $l/h = 22, 62, 90, 180,$ and 840 in Fig. S4 and Table S1 in Ref. [26] at l/h from 62 to 960 and various Wi. The results confirm the observation reported in Ref. [21], where DSR is observed only at chaotic E_u interacting with a flat, white noise E_w accompanied by weak elastic waves.

Here we intend to clarify the difference between flat, white noise and chaotic power spectra. The main feature of a white noise power spectrum is the frequency independence of an average spectrum intensity, where the noise fluctuation amplitude value is defined by the average spectrum intensity. The larger the average intensity, the larger the noise fluctuation amplitudes around average spectrum intensity. Moreover, the peak intensity of elastic waves appearing in the spanwise velocity spectrum, E_w, strongly depends on $\mathrm{Wi} - \mathrm{Wi}_c$ and increases from zero at Wi_c to higher values. Thus, the elastic wave wide peak with intensity growing from zero occurs on the top of flat E_w, clearly seen at $l/h = 675$ and $\mathrm{Wi} = 168$ and 233 in the lower subrange, where flat E_w slightly bends up by low-intensity elastic wave peaks for both Wi values (see Fig. 3). At higher Wi values in the upper subrange of the transition flow regime, the elastic wave peaks become more pronounced but still remain wide and their slopes at high frequencies decay more sharplywith increasing Wi. It is the main distinctive feature of a chaotic flow power spectrum.

Further on, we notice that an appearance of flat E_w depends, besides Wi, also on l/h: the closer to the channel inlet, the larger the streamwise velocity fluctuations, u_{rms}, and the more pronounced the E_w power-law decay, as seen in Figs. S3(a) and S4(a)–S4(c) in Ref. [26]. For example, at $l/h = 22$, E_w looks similar to chaotic E_u for all Wi values throughout the transition regime, and DSR is absent, as shown in Fig. S4(a) in Ref. [26], whereas, at $l/h = 62$ and 90, E_w becomes chaotic at all $\mathrm{Wi} > \mathrm{Wi}_c$, except at $\mathrm{Wi} = 162$ and 160, respectively, where E_w is nearly flat. The deviation of E_w from a flatness occurs, since its intensity is below the resolution bound, presented in Fig. S5 in Ref. [26]. Thus, the DSR emerges only in the lower subrange, where the flat, white noise E_w is observed, as shown in the phase diagram in Wi and l/h coordinates in Fig. 4. This is the major finding, first reported at $l/h = 380$ in Ref. [21].

The reason for the l/h dependence of the Wi value of the upper bound of the lower subrange, where DSR appears, is the normalized rms of streamwise velocity fluctuations, u_{rms}/U, decaying along the channel, l/h, at all Wi in the transition flow regime: sharp decrease from the inlet $l/h = 0$ up to $l/h \leqslant 90$ and further on just a weak depletion until the outlet [see Fig. S3(a) in Ref. [26]].

Similarly to u_{rms}/U, $I_{\mathrm{el}}/w_{\mathrm{rms}}^2$ decreases along the channel, where I_{el} is the peak intensity of the elastic wave above the E_w flat power spectrum, as presented for this channel at $l/h = 380$ [21]. The first observation of $I_{\mathrm{el}}/w_{\mathrm{rms}}^2$ is reported in a channel with nonsmooth inlet and six small holes in a top plate, shown in Fig. 6 of Ref. [3], and in Fig. S3 in Ref. [26] for the current channel. Thus, in contrast to Newtonian open flows, the viscoelastic channel flow properties depend on l/h above Wi_c, in Fig. S3 in Ref. [26]. Moreover, the u_{rms}/U dependence on l/h is the same for the lower and upper subranges, as seen in Fig. S3(a) in Ref. [26], while the dependence of $I_{\mathrm{el}}/w_{\mathrm{rms}}^2$ on l/h is different in the lower and upper subranges, shown in Fig. S3(b) in Ref. [26]. Furthermore, both u_{rms}/U and $I_{\mathrm{el}}/w_{\mathrm{rms}}^2$ show two distinct regions with similar l/h dependencies: a steep decrease near the inlet and a gentle depletion further away. Near the inlet, the steep decrease of u_{rms}/U occurs from $l/h = 0$ at about 14% down to ≈4% at $l/h \approx 90$ and then gentle depletion to ≈3% at the outlet, whereas for $I_{\mathrm{el}}/w_{\mathrm{rms}}^2$ the transition location from steep to gentle slope takes place for the lower subrange at $l/h \approx 140$ and for the upper subrange at $l/h \approx 90$; as a result, the steepness for $I_{\mathrm{el}}/w_{\mathrm{rms}}^2$ differs for the lower and upper subranges far from the inlet Fig. S3(b) in Ref. [26]. Thus, the observed dependence of the DSR existence range and the elastic wave intensity on l/h is due to the dependence of u_{rms}/U on l/h, hence u_{rms}/U is the second control parameter besides Wi. It means that different u_{rms}/U values at the inlet, $l/h = 0$, should also affect the existence range of flat, white noise E_w, and so the DSR appearance.

To summarize, the DSR discovery reported recently is found at a single channel location, $l/h = 380$, in the lower subrange just above Wi_c, and its existence is defined only by Wi [21]. Here we show a strong dependence of Wi value of the lower subrange upper bound on l/h downstream of the inlet. At $l/h = 22$ and $\mathrm{Wi} = 162$ and 235, u_{rms}/U is larger by a factor of about 4, compared with at $l/h = 62$ and $\mathrm{Wi} = 235$, while u_{rms}/U is only about twice larger. Such large u_{rms}/U values result in chaotic E_w and much larger I_{el} values for all $\mathrm{Wi} > \mathrm{Wi}_c$ at $l/h = 22$. However, at $l/h = 62$ and 90 and $\mathrm{Wi} = 162$, E_w remains flat with I_{el} values below the resolution limit, marked by the red dotted line in Fig. S6(b) in Ref. [26], and the existence of the DSR and flat, white noise E_w depends on the u_{rms}/U values. Thus, the coherent interaction of chaotic spectrum E_u, flat white-noise spectrum E_w, and weak elastic waves results in the enhanced response realized as DSR.

In conclusion, at a given intensity of external white noise at the inlet, DSR appears exclusively in the lower subrange of the transition flow regime with the Wi value of the upper bound depending on l/h downstream along the channel. We identify three key factors required for the appearance of DSR as a function of Wi and u_{rms}/U: (i) chaotic E_u, (ii) flat white-noise E_w, and (iii) low-intensity elastic waves, as reported first at $l/h = 380$ in Ref. [21]. As shown in Fig. S3(a) in Ref. [26], the u_{rms}/U value depends on l/h and plays the role of the second control parameter besides Wi. When E_w becomes chaotic, DSR ceases to exist, because the required three conditions of the mechanism for the DSR generation are no longer satisfied. The next important result is the same scaling exponents within the error bars of the power-law fits of DSR and elastic wave frequencies, λf_p and λf_{el}, as a function of $\mathrm{Wi} - \mathrm{Wi}_c$, which proves the direct relation between DSR and elastic waves, although λf_p is shifted down by a factor of 4–5 relative to λf_{el}. Thus, these two basic findings are the critical ingredients indicating similar conditions of the DSR observation in the autonomous deterministic dynamical chaotic system, where the chaotic attractor interacts with external δ-correlated white noise in the presence of limit cycles (oscillations). It is worth recalling that at $l/h = 380$ the direct connection between the observations of DSR in the 3D channel flow and deterministic chaotic system is the presentation of the 3D flow dynamics in $(u^p_{\mathrm{rms}})^2$ versus $(w^p_{\mathrm{rms}})^2$ presentation in the transition flow regime in Ref. [21]. We should also emphasize that our experimental observations are obtained in a flow with infinite degrees of freedom, in contrast to the autonomous deterministic dynamical chaotic model [22,23].

We thank Guy Han and Rostyslav Baron for their help with the experimental setup. This work was supported by the Scientific Research Innovation Capability Support Project for Young Faculty (Grant No. ZYGXQNJSKYCXNLZCXM-O1), the National Natural Science Foundation of China (Grant No. 12472255), the Fundamental Research Funds for the Central Universities (Grant No. 3072025CFJ0102), the High-Level International Cooperation Cultivation Fund of Harbin Engineering University, and the Israel Science Foundation (Grant No. 784/19).

[1] N. K. Jha and V. Steinberg, Elastically driven Kelvin–Helmholtz-like instability in straight channel flow, Proc. Natl. Acad. Sci. USA **118**, e2105211118 (2021).

[2] R. Shnapp and V. Steinberg, Nonmodal elastic instability and elastic waves in weakly perturbed channel flow, Phys. Rev. Fluids **7**, 063901 (2022).

[3] Y. Li and V. Steinberg, Universal properties of non-Hermitian viscoelastic channel flows, Sci. Rep. **13**, 1064 (2023).

[4] Y. Li and V. Steinberg, Mechanism of vorticity amplification by elastic waves in a viscoelastic channel flow, Proc. Natl. Acad. Sci. USA **120**, e2305595120 (2023).

[5] V. A. Gorodtsov and A. I. Leonov, On a linear instability of a plane parallel Couette flow of viscoelastic fluid, J. Appl. Math. Mech. **31**, 310 (1967).

[6] M. Renardy and Y. Renardy, Linear stability of plane couette flow of an upper convected maxwell fluid, J. Non-Newtonian Fluid Mech. **22**, 23 (1986).

[7] K. C. Lee and B. A. Finlayson, Stability of plane poiseuille and Couette flows of a maxwell fluid, J. Non-Newtonian Fluid Mech. **21**, 65 (1986).

[8] T. C. Ho and M. Denn, Stability of plane poiseuille flow of a highly elastic liquid, J. Non-Newtonian Fluid Mech. **3**, 179 (1977).

[9] M. Avila, D. Barkley, and B. Hof, Transition to turbulence in pipe flow, Annu. Rev. Fluid Mech. **55**, 575 (2023).

[10] Y. Li and V. Steinberg, Properties of low-inertia viscoelastic channel flow with smoothed inlet, Phys. Rev. Fluids **9**, 113302 (2024).

[11] M. Khalid, V. Shankar, and G. Subramanian, Continuous pathway between the elasto-inertial and elastic turbulent states in viscoelastic channel flow, Phys. Rev. Lett. **127**, 134502 (2021).

[12] G. Buza, J. Page, and R. R. Kerswell, Weakly nonlinear analysis of the viscoelastic instability in channel flow for finite and vanishing reynolds numbers, J. Fluid Mech. **940**, A11 (2022).

[13] M. M. Couchman, M. Beneitez, J. Page, and R. R. Kerswell, Inertial enhancement of the polymer diffusive instability, J. Fluid Mech. **981**, A2 (2024).

[14] T. Lewy and R. Kerswell, The polymer diffusive instability in highly concentrated polymeric fluids, J. Non-Newtonian Fluid Mech. **326**, 105212 (2024).

[15] M. Lellep, M. Linkmann, and A. Morozov, Purely elastic turbulence in pressure-driven channel flows, Proc. Natl. Acad. Sci. USA **121**, e2318851121 (2024).

[16] E. S. G. Shaqfeh, Purely elastic instabilities in viscometric flows, Annu. Rev. Fluid Mech. **28**, 129 (1996).

[17] P. Pakdel and G. H. McKinley, Elastic instability and curved streamlines, Phys. Rev. Lett. **77**, 2459 (1996).

[18] V. Steinberg, Elastic turbulence: An experimental view on inertialess random flow, Annu. Rev. Fluid Mech. **53**, 27 (2021).

[19] A. Varshney and V. Steinberg, Elastic Alfven waves in elastic turbulence, Nat. Commun. **10**, 652 (2019).

[20] M. V. Kumar, A. Varshney, D. Li, and V. Steinberg, Relaminarization of elastic turbulence, Phys. Rev. Fluids **7**, L081301 (2022).

[21] Y. Li and V. Steinberg, From laminar to chaotic flow via stochastic resonance in viscoelastic channel flow, Phys. Rev. Res. **6**, 043260 (2024).

[22] V. S. Anishchenko, A. B. Neiman, and M. A. Safanova, Stochastic resonance in chaotic systems, J. Stat. Phys. **70**, 183 (1993).

[23] V. S. Anishchenko, A. B. Neiman, F. Moss, and L. Shimansky-Geier, Stochastic resonance: Noise-enhanced order, Phys. Usp. **42**, 7 (1999).

[24] R. Benzi, A. Sutera, and A. Vulpiani, The mechanism of stochastic resonance, J. Phys. A **14**, L453 (1981).

[25] L. Gammaitoni, P. Hänggi, P. Jung, and F. Marchesoni, Stochastic resonance, Rev. Mod. Phys. **70**, 223 (1998).

[26] See Supplemental Material at http://link.aps.org/supplemental/10.1103/yv5x-261v for methods details and the supplemental figures and table, which includes Refs. [27,28].

[27] Y. Liu, Y. Jun, and V. Steinberg, Concentration dependence of the longest relaxation times of dilute and semi-dilute polymer solutions, J. Rheol. **53**, 1069 (2009).

[28] A. Liberzon, T. Käufer, A. Bauer, P. Vennemann, and E. Zimmer, Openpiv/openpiv-python: Openpiv-python v0.23.3, Zenodo (2020), 10.5281/zenodo.4320056.